2020 Fifteenth International Conference on Ecological Vehicles and Renewable Energies (EVER)

# Core Temperature Estimation for a Cylindrical Cell Battery Module

Rath, S. (Subhajeet), Hoedemaekers, E.R.G. (Erik) and Wilkins, S. (Steven)
Traffic and Transport Unit
Nederlandse Organisatie voor Toegepast Natuurwetenschappelijk Onderzoek (TNO)
Helmond, Netherlands
Email: subhajeet.rath@tno.nl; erik.hoedemaekers@tno.nl; steven.wilkins@tno.nl

***Abstract*—Lithium ion (Li-ion) batteries in electric vehicle (EV) applications must operate within a narrow temperature range to ensure safety, performance and longevity. Hence, advanced thermal management strategies should have access to internal cell temperatures in a battery pack. In real world application, surface temperatures can be measured, but it is difficult to place a sensor at the core (which can be more than 10°C higher that the surface) due to the added cost and intrusive nature.**

**In this paper, a pack level thermal model is developed for a cylindrical cell battery module which is modular and scalable. This model is used in a Kalman filter based Thermal State Observer (TSO) which is constructed to be real-time capable for application in a Battery Management System (BMS). The TSO uses limited cell surface measurements to estimate the core temperature of the full battery pack. The paper also discusses the methodology for characterization and validation of the thermal model and TSO.**

***Index Terms*—Battery Core Temperature Estimation; Battery Thermal Model; Thermal State Observer; Thermal Fault Handeling.**

## I. Introduction

Past few decades have seen a rapid increase in global energy consumption resulting in deteriorating environmental conditions. A major contributor to these issues is the transportation sector [1]. This has led to an increased interest towards vehicle electrification.

Lithium ion (Li-ion) batteries are currently considered the most viable form of energy storage for electric vehicle (EV) due to high energy density, charge efficiency and cycle life. However, they have a narrow operating temperature range, which require accurate battery temperature prediction to ensure safety, performance, and longevity.

Existing battery management systems (BMS) typically use a temperature sensor mounted to the surface of the cell, the measurement from which is assumed to be the cell internal temperature. However, under typical operating conditions, such as a standard Hybrid Electric Vehicle (HEV) drive cycle, cells may experience temperature differences of more than 10°C between surface and core [2].

Core temperature can be measured via embedded micro-temperature sensors within the cell [3], [4]. However, the additional manufacturing challenges and instrumentation requirements of this approach would significantly increase cost and complexity, especially when applied to a battery pack with a large number of cells.

Several research give a technique for sensorless estimation of core temperature based on electrochemical impedance [5]–[7]. While these methods show good promise for individual cell temperature estimation in lab conditions, it is challenging to implement the same onboard a vehicle due to cumbersome instrumentation and software requirements [6]. Additionally, the demonstrated methods require impedance measurement and surface temperature of every cell, which is difficult for large battery packs [5].

Another way to approach the problem is to employ a Model based temperature estimation. Existing high fidelity thermal models can predict a detailed temperature distribution throughout a cell [8], [9]. However, these models are not suitable for onboard application due to their high computational intensity. Reduced order models use the bulk (or average) temperature to capture the lumped thermal dynamics of a cell [10], [11]. Such simplified models are computationally efficient for onboard applications due to having smaller number of states. Lumped thermal models capturing both the surface and the core temperatures of a cell have been studied in [2] and [12], while [16] extends them to model a string consisting of multiple cells. These studies can be used to model a complete battery pack and use temperature measurements at selected locations to estimate the core temperature of every cell.

The rest of the paper is divided into the following Sections. In Section II the thermal model for the com-

978-1-7281-5641-5/20/$31.00 ©2020 European Union

plete battery pack is developed. Section III gives the framework of a Thermal State Observer (TSO) based on the thermal model. In Section IV the parameters required in the thermal model are identified by various methods. Section V gives a reduced order model which is useful for an automotive application. In Section VI, the performance of the thermal model and TSO is discussed and Section VII gives the final conclusion.

## II. Thermal Model

In this section, a mathematical model describing the thermal behaviour of a battery pack is discussed. This model is formulated for a prototype battery module which was manufactured in-house and was used for testing and validation purposes. The model is described in a scalable and modular manner, such that changes in layout and number of cells can be accommodated.

### A. Prototype Battery Module

Fig. 1 shows the prototype battery module. It consists of 36 cylindrical cells arranged twelve in series and three in parallel. These cells are 21700 format with NMC chemistry. The pack is liquid cooled, where the coolant can be circulated via two aluminium cooling plates (top and bottom).

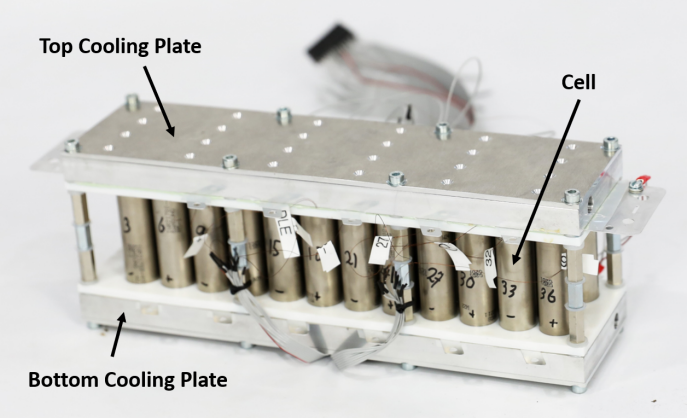


Fig. 1: Battery module prototype.

### B. Mathematical Model

Fig. 2 shows the structure of a single cell. It has a core and surface with heat capacities $C_c$ and $C_s$ respectively. Hence, the total heat capacity of the cell is $C_{cell} = C_c + C_s$. These thermal masses are connected to each other by a thermal resistance $R_{cs}$. The core and surface temperatures are $T_i^c$ and $T_i^s$ respectively, where $i$ is the index of the cell within the module (as shown in Fig. 3).

Fig. 3 shows the planer hexagonal arrangement of the cells in the battery module shown in Fig. 1. Each cell has six neighbour, which is either an adjacent cell or the ambient. Fig. 3 also highlights Cell 9 in blue and marks it's neighbours: four cells 6, 8, 11 and 12 (shown in green) and two ambient points (shown in black).

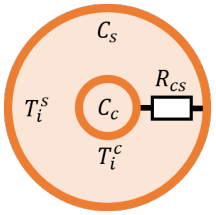


Fig. 2: Structure of a single cell.

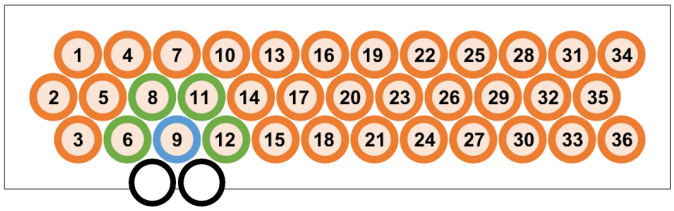


Fig. 3: Arrangement of cells in the battery module (Top View).

Fig. 4 shows the thermal inter-connections of Cell 9 with its surroundings. The surface of Cell 9 is connected to the surface of it's neighbouring cells and ambient with thermal resistance of $R_{ss}$ and $R_{sa}$ respectively (Fig. 4a). It is connected to the top and bottom cooling plate with thermal resistance of $R_{sp}$ (Fig. 4b). The cooling plates have a heat capacity of $C_p$ and thermal resistance of $R_{Ta}$ and $R_{Ba}$ respectively to ambient. The ambient temperature is denoted by $T^a$.

Thermal dynamics of Cell 9 can be derived by considering all the heat flow paths through the core and the surface. For the core, there is heat flow from core to surface and internal heat generation due to electrical resistance of the cell. The governing equation is shown as (1), where $\dot{Q}_9$ gives the internal heat released by Cell 9. For the surface, there is heat flow from surface to core, adjacent cells, ambient and cooling plates. The governing equation is (2).

$$C_c \dot{T}_9^c = \frac{T_9^s - T_9^c}{R_{cs}} + \dot{Q}_9 \tag{1}$$

$$\begin{aligned} C_s \dot{T}_9^s = & \frac{T_9^c - T_9^s}{R_{cs}} + \frac{T_6^s - T_9^s}{R_{ss}} + \frac{T_8^s - T_9^s}{R_{ss}} \\ & + \frac{T_{11}^s - T_9^s}{R_{ss}} + \frac{T_{12}^s - T_9^s}{R_{ss}} + 2\frac{T_a - T_9^s}{R_{sa}} \\ & + \frac{T_T^p - T_9^s}{R_{ps}} + \frac{T_B^p - T_9^s}{R_{sp}} \end{aligned} \tag{2}$$

Similarly, thermal dynamics of top and bottom cooling plate can be derived by considering heat flow from the

plate to cells and ambient, and heat removed by the cooling fluid. Equation (3) and (4) show the thermal dynamics of top and bottom cooling plate respectively. Here, $\dot{Q_T}$ and $\dot{Q_B}$ give the heat removed by the coolant from top and bottom cooling plate respectively.

$$C_p\dot{T_T^p} = \sum_{i=1}^{n_{cell}} \frac{T_i^s - T_T^p}{R_{sp}} + \frac{T_a - T_T^p}{R_{Ta}} - \dot{Q_T} \quad (3)$$

$$C_p\dot{T_B^p} = \sum_{i=1}^{n_{cell}} \frac{T_i^s - T_B^p}{R_{sp}} + \frac{T_a - T_B^p}{R_{Ba}} - \dot{Q_B} \quad (4)$$

The thermal interconnection for every cell is unique and dependant upon its location. This gives different equation for each temperature state. Applying the generic scheme of (1) and (2) to all the cells, resulting governing equations can be derived as (5) and (6). The equations for top and bottom cooling plates can be taken from (3) and (4) and written as (7) and (8). Equation (5) to (8) define the state-space formulation of thermal dynamics of the battery module.

### C. Electrical Model

The internal heat generation of the battery is a consequence of it's electrical behaviour. A separate model is derived to compute that for each cell. When current $I_i$ passes through the $i^{th}$ cell of the battery, cell voltage $U_i$ deviates from the open circuit voltage $V_i^{oc}$ because of electrochemical polarization [13]. The resulting energy loss is converted into heat. Here, the heat generation due to this overpotential can be expressed as

$$\dot{Q_i^P} = (U_i - V_i^{oc})\, I_i \quad (9)$$

The entropic heat generation caused by the change in entropy [13] is expressed as

$$\dot{Q_i^S} = I_i T_i \frac{d}{dT_i} V_i^{oc} \quad (10)$$

Here, $T_i$ is the cell temperature and $dV_i^{oc}/dT_i$ is the entropic heat coefficient. The total internal heat generation of a cell is calculated as

$$\dot{Q_i} = \dot{Q_i^P} + \dot{Q_i^S} \quad (11)$$

### D. Cooling Model

The heat removed by the coolant ($\dot{Q_T}$ and $\dot{Q_B}$) can be calculated by modelling it's interaction with the cooling plate. From Fig. 5 it can be seen that the top cooling plate has an S-shaped channel through which the fluid passes. This is approximated as a straight pipe having equivalent orifice area ($A_{ch}$) and channel length ($L_{ch}$) passing through the plate which acts as a wall of uniform temperature (Fig. 5).

Fig. 6 shows a segment in the cooling plate channel of thickness $dx$ at a length $x$ from the inlet. The coolant removes heat from the cooling plate via convection and brings about an increase in it's temperature. This is expressed as

$$\dot{V}\rho c_p dT^f = hA_{ch}\left(T_T^p - T^f\right) dx \quad (12)$$

where $\dot{V}$, $\rho$ and $c_p$ are the flow rate, density and specific heat capacity of the coolant, $T^f$ and $dT^f$ are the temperature and the increase in temperature of the cooling fluid at $x$, and $h$ is the convective heat transfer co-efficient.

An integral over the entire length of the channel can be defined as

$$\int_{T_{in}^f}^{T_{out}^f} \frac{1}{T_T^p - T^f} dT^f = \int_0^{L_{ch}} \frac{hA_{ch}}{\dot{V}\rho c_p} dx \quad (13)$$

where $T_{in}^f$ and $T_{out}^f$ are temperatures of the fluid at inlet and outlet. Evaluation of this integral gives

$$-\ln\left|\frac{T_T^p - T_{out}^f}{T_T^p - T_{in}^f}\right| = \frac{1}{\dot{V}\rho c_p R_{pf}} \quad (14)$$

where $R_{pf} = 1/hA_{ch}L_{ch}$ is an equivalent thermal resistance between plate and fluid. The total heat removed by the coolant from top cooling plate due to it's specific heat capacity can be calculated as

$$\dot{Q_T} = \dot{V}\rho c_p\left(T_{out}^f - T_{in}^f\right) \quad (15)$$

Substituting (14) into (15), the heat removed by top cooling plate is given by (16). Similarly, heat removed by bottom cooling plate can be derived as (17).

$$\dot{Q_T} = \dot{V}\rho c_p\left(T_T^p - T_{in}^f\right)\left(1 - e^{-1/(\dot{V}\rho c_p R_{pf})}\right) \quad (16)$$

$$\dot{Q_B} = \dot{V}\rho c_p\left(T_B^p - T_{in}^f\right)\left(1 - e^{-1/(\dot{V}\rho c_p R_{pf})}\right) \quad (17)$$

## III. Thermal State Observer

For a commercially available cylindrical cell, it is extremely difficult to measure the temperature of its core. A sensor based measurement generally involves irreversible modification to the cell, such as drilling, punching etc. However, with the knowledge about the behaviour of the battery module, the core temperature can be estimated by surface temperature measurements. This is accomplished by designing a Kalman Filter based Thermal State Observer for the thermal model described in Section II-B.

$$\dot{T}_i^c = -\frac{T_i^c}{R_{cs}C_c} + \frac{T_i^s}{R_{cs}C_c} + \frac{\dot{Q}_i}{C_c} \tag{5}$$

$$\dot{T}_i^s = \frac{T_i^c}{R_{cs}C_s} - \left[\frac{1}{R_{cs}C_s} + \frac{n_s}{R_{ss}C_s} + \frac{n_a}{R_{sa}C_s} + \frac{2}{R_{sp}C_s}\right] T_i^s + \sum_{j\in\text{adjecent cells}} \frac{T_j^s}{R_{ss}C_s} + \frac{T_T^p}{R_{ps}C_s} + \frac{T_B^p}{R_{sp}C_s} + n_a\frac{T_a}{R_{sa}C_s} \tag{6}$$

$$\dot{T}_T^p = \sum_{i=1}^{n_{cell}} \frac{T_i^s}{R_{sp}C_p} - \left[\frac{n_{cell}}{R_{sp}C_p} + \frac{1}{R_{Ta}C_p}\right] T_T^p + \frac{T_a}{R_{Ta}C_p} - \frac{\dot{Q}_T}{C_p} \tag{7}$$

$$\dot{T}_B^p = \sum_{i=1}^{n_{cell}} \frac{T_i^s}{R_{sp}C_p} - \left[\frac{n_{cell}}{R_{sp}C_p} + \frac{1}{R_{Ba}C_p}\right] T_B^p + \frac{T_a}{R_{Ba}C_p} - \frac{\dot{Q}_B}{C_p} \tag{8}$$

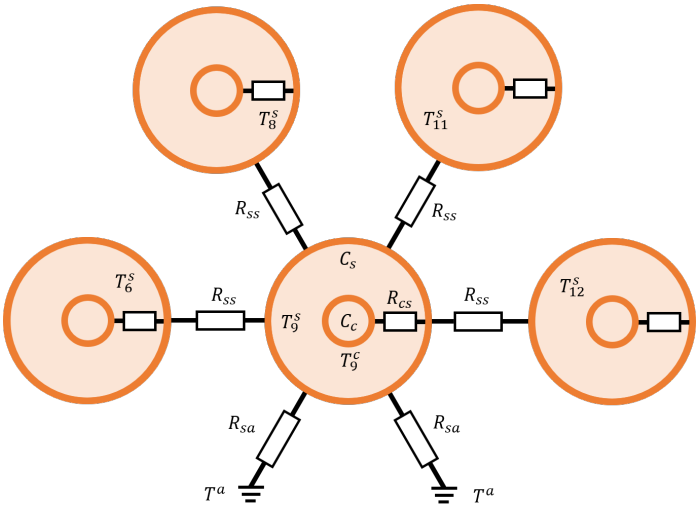


(a) Top View

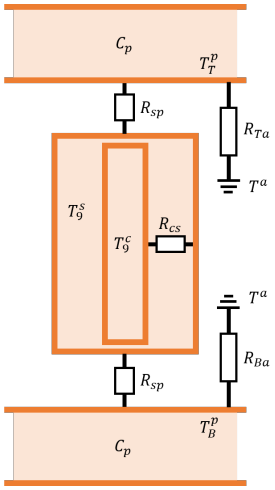


(b) Side View

Fig. 4: Thermal inter-connections of Cell 9.

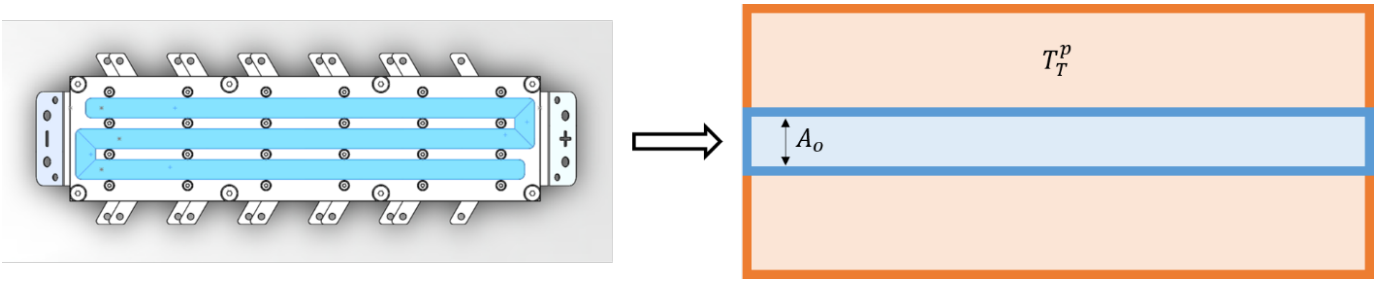


Fig. 5: Representation of Top Cooling Plate.

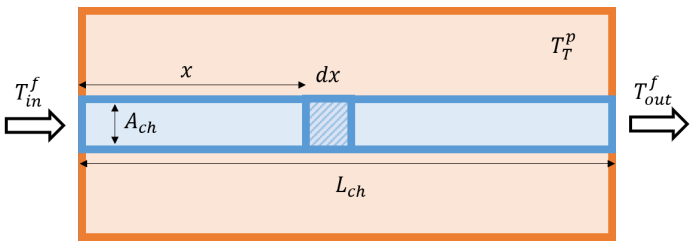


Fig. 6: Thermal Modelling for Top Cooling Plate.

### A. Kalman Filter

The Kalman Filter was developed by Rudolf E. Kalman around 1960 [15]. It is a state estimator which produces an optimal estimate by minimizing the mean value of the sum of estimation errors. The algorithm was originally developed for linear state-space model, however the Extended Kalman filter also works for non-linear system. In this study, the Kalman filter will be implemented for the battery model which is a linear state-space system.

A generic discrete time linear state-space system can be defined as (18) and (19). Here, $x$ denotes the state, $u$ the input and $y$ the measured signals. It is assumed that the system is excited by random ("white") disturbances (process noise) and the measurements contain random ("white") measurement noise. The process noise is characterised by $Gw$ and measurement noise by $v$, where $w$ and $v$ are assumed to be white noise with auto-covariance matrix $Q$ and $R$ respectively.

$$x(n+1) = Ax(n) + Bu(n) + Gw(n) \quad (18)$$
$$y(n) = Cx(n) + Du(n) + v(n) \quad (19)$$

The Kalman Filter is initialized with an estimated initial state $\hat{x}(0) = x_{init}$ and estimated initial state uncertainty $\hat{P}(0) = \hat{P}_{init}$. These can be arbitrarily assigned. At a time step $n$, the system is supplied with measurement $y(n)$. The Kalman gain $(K)$ is then calculated as

$$K(n) = \hat{P}(n)C^T[C\hat{P}(n)C^T + R]^{-1} \quad (20)$$

and is used to improve the estimated state and estimation uncertainty as

$$\hat{x}^+(n) = \hat{x}(n) + K(n)(y(n) - C\hat{x}(n) - Du(n))$$
$$\hat{P}^+(n) = [I - K(n)C]\hat{P}(n)$$

A new system state and state uncertainity is predicted for the next time step by using the corrected estimated state and estimation uncertainty as

$$\hat{x}(n+1) = \hat{x}^+(n) + (A\hat{x}^+(n) + Bu(n)) \quad (21)$$
$$\hat{P}(n+1) = A\hat{P}^+(n)A^T + GQG^T \quad (22)$$

These values are used in the next iteration to estimate the system state and calculate the estimation uncertainty again.

## IV. System Identification

In this section the parameters required in the battery thermal model are identified by conducting several tests. Some parameters are also inferred from their material properties. These parameters are summarised in Table. I.

### A. Cell Calorimetry Test

In this test an Accelerating Rate Calorimeter (ARC) is used to add a known amount of heat adiabatically to a cell and record it's temperature rise. Dividing this heat input by the temperature difference gives the thermal capacity of the cell ($C_{cell}$) which is found as $60.5\,\mathrm{J\,K^{-1}}$. This data can be further used to calculate the thermal capacity of the cell's surface and core.

TABLE I: Battery thermal model parameters.

| Parameter | Value | Unit |
|---|---|---|
| $C_{cell}$ | 60.5 | J/K |
| $C_c$ | 51.35 | J/K |
| $C_s$ | 9.15 | J/K |
| $C_p$ | 777.6 | J/K |
| $R_{cs}$ | 0.6 | K/W |
| $R_{ss}$ | 500 | K/W |
| $R_{sp}$ | 15 | K/W |
| $R_{sa}$ | 190 | K/W |
| $R_{Ta}$ | 0.02 | K/W |
| $R_{Ba}$ | 1.36 | K/W |
| $R_{pf}$ | 0 | K/W |

### B. Parameter identification from material property

Table II give several components whose thermal capacities are derived from their material properties. The thermal capacity of a cell is known from the Calorimetry test. Casing of the cell is representative of the cell surface. It's mass and specific heat capacity can be found from the manufacturer's data sheet. The thermal capacity of cell surface ($C_s$) can be found as $9.15\,\mathrm{J\,K^{-1}}$. Thermal capacity of cell core ($C_c$) is the difference between thermal capacities of cell and surface, and is calculated as $51.35\,\mathrm{J\,K^{-1}}$.

Similarly, the thermal capacity of cooling plate is also found from it's material properties. The cooling plate assembly comprises of three components: cooling block, cooling lid and gap filler. The calculation of thermal capacity of these components are given in Table II. Thermal capacity of cooling plate is calculated as $777.6\,\mathrm{J\,K^{-1}}$.

TABLE II: Heat capacities of different components.

| Part | Material | Weight [Kg] | Specific heat [J/kg/K] | Thermal capacity [J/K] |
|---|---|---|---|---|
| **Cell** | | | | 60.50 |
| Cell Surface | SS 304 | 0.0176 | 520 | 9.15 |
| Cell Core | | | | 51.35 |
| **Cooling Plate** | | | | 777.60 |
| Cooling Block | Alu 7075 | 0.6030 | 960 | 578.88 |
| Cooling Lid | Alu 6063 | 0.1930 | 900 | 173.70 |
| Gap filler | Silicone | 0.0351 | 712 | 25.02 |

The coolant used in the module is 50:50 glycol:water mix. It has a density ($\rho$) and heat capacity ($c_p$) of $1084.5\,\mathrm{kg\,m^{-3}}$ and $3.14 \times 10^3\,\mathrm{J\,kg^{-1}\,K^{-1}}$ respectively.

### C. Cell Heating Test

This test is conducted to identify various thermal resistances in the model. In this test, the module is subjected to a current profile which facilitates a constant generation of battery internal heat for a significantly long time to allow all cell temperatures to stabilize (reach

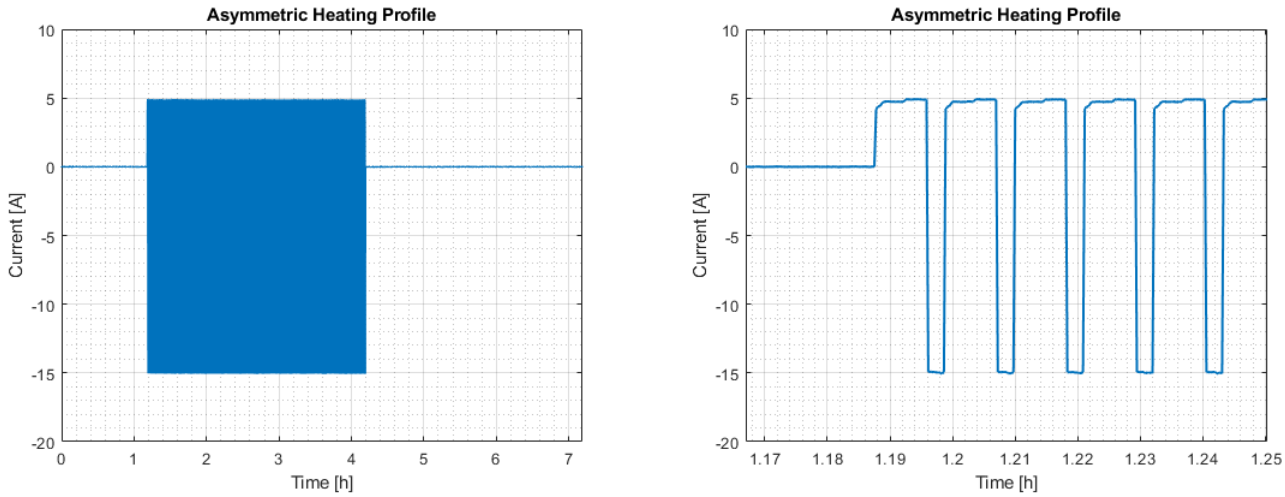


(a) Full View

(b) Zoomed View

Fig. 7: Current profile for Cell Heating Test.

steady-state). The module is operated at $50\,\%$ SoC with a current profile that doesn't change the SoC significantly. This is done to ensure that cells/module is least likely to reach any limitations that could influence/change the amount of heat generated (e.g. different internal resistance at low/high SoC). Fig. 7 shows the current profile for this test, where the module is alternatively subjected to a maximum charge ($15\,\mathrm{A}$) and discharge ($45\,\mathrm{A}$) step current. Length of the pulse is set such that the amount of charge removed and gained during the charge and discharge step are equal.

A fixed cooling is applied to the setup by circulating the coolant at a temperature of $10\,^{\circ}\mathrm{C}$ and at a flow rate of $8.333 \times 10^{-5}\,\mathrm{m^3\,s^{-1}}$. The coolant is only circulated through the top cooling plate (limitation of the setup). The test is conducted at $0\,^{\circ}\mathrm{C}$, $20\,^{\circ}\mathrm{C}$ and $40\,^{\circ}\mathrm{C}$ ambient, and temperatures of Cell 20, 21, 27 and 36, the top and bottom cooling plate are measured. The thermal resistances are tuned such that the error between measured and simuated temperatures for these cells and cooling plates are minimized for all ambient conditions. From this test, the following parameters can be identified: $R_{ss}$, $R_{sp}$, $R_{sa}$, $R_{Ta}$, $R_{Ba}$ and $R_{pf}$. The results at $20\,^{\circ}\mathrm{C}$ ambient for Cell 20 and 27 is shown in Fig. 8.

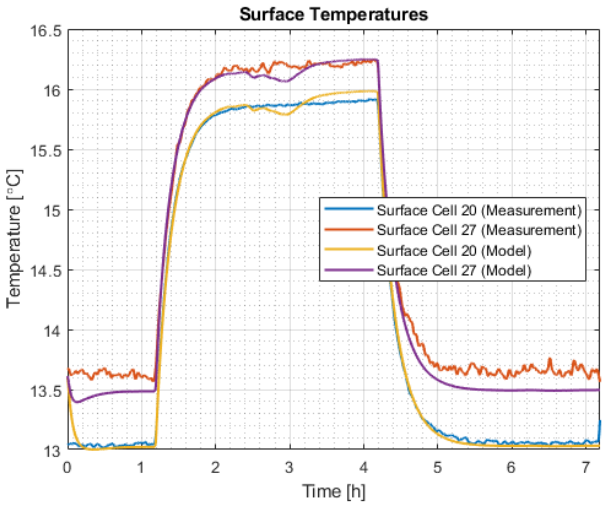


Fig. 8: Cell Heating Test at $20\,^{\circ}\mathrm{C}$ ambient.

### *D. FEM simulation of a cell*

As the developed prototype module does not include measurements of the core temperature of the cells but the model includes them, a 3D FEM model was used to generate the data needed to calibrate the corresponding parameter ($R_{cs}$). Since, the modelling of core temperature dynamics is identical for every cell, FEM simulation of one cell can generate the required data. This data consists of four measurement points around the circumference of the cell, one on each terminal of the cell and one in the core of the cell. The sensor locations are shown in Fig. 9.

The 3D FEM model is initialized with every component at the same temperature of 20°C (equal to the ambient temperature in the simulation), additionally the heat generation of each cell is set to 1W. The internal heat transfer coefficients for the battery cells are not a trivial material property, since the inside of a cell consist of a 'jelly-roll' of electrodes and separator material. The material properties and typical dimensions are taken from [14]. The thermal conductivities used in the FEM model are calculated as:

- Tangential thermal conductivity: $0.72\,\mathrm{W\,m^{-1}\,K^{-1}}$
- Axial thermal conductivity: $31.52\,\mathrm{W\,m^{-1}\,K^{-1}}$

The FEM model of the cell is simulated with these

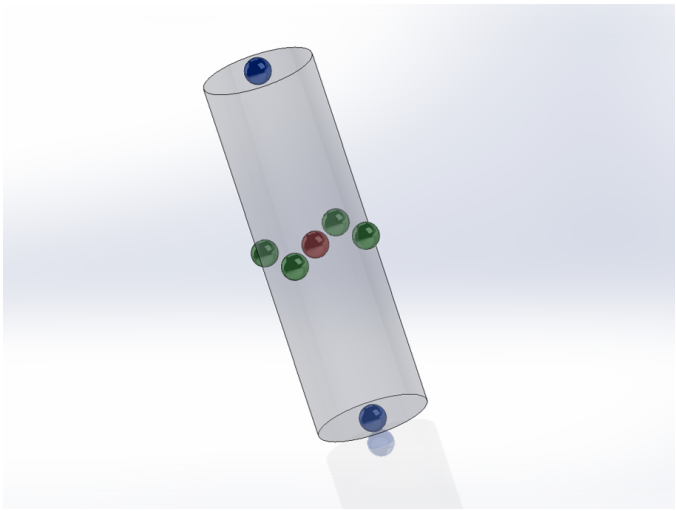

(a) Temperature measurement locations.

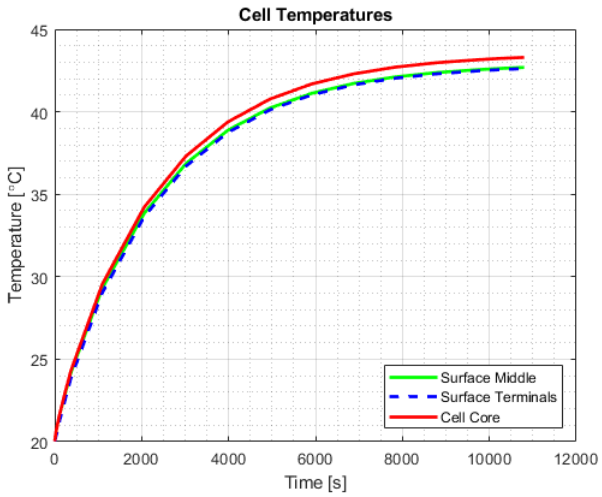


(b) Temperature simulation.

Fig. 9: FEM simulation of a single cell.

settings and the relevant data is extracted (shown in Fig. 9b). The thermal resistance between core and surface is calculated as $0.6\,\mathrm{K\,W^{-1}}$.

## V. Model Reduction

As discussed in Section II-B, (5) to (8) give the state-space equations describing the thermal dynamics of the battery module. This state-space model can be leveraged in a Kalman Filter based Thermal State Observer to estimate the core and surface temperatures of the battery. The TSO makes use of large matrix multiplications involving system matrices and it is desirable to keep them small for faster computation.

For the model under consideration, a new equation for the dynamics of the surface temperature can be derived as (23) by decoupling it from the core temperature. Here, the entire thermal mass of the cell is taken on the surface and any interaction from the core is neglected. Equation (23), (7) and (8) are the new state-space equations and the core temperature can be calculated separately using (5). The model reduction significantly reduces the computational complexity and improves the observability of the system.

The new model improves the computation time without affecting the performance of the system. For this type of battery system, core temperature measurements are absent in most practical applications. Hence, it is not required to be included as a state to be used in the TSO for comparision to a measured signal. Additionally, the core temperature is dependent on only one state, which is the surface temperature of the corresponding cell. These are connected by a thermal resistence which is identified to be very small. This also emsures that the core and surface have fairly similar dynamics, which can be captured with good accuracy by the reduced order model. The reduced order model also improves the observability of the system as lower number of measurements are required to make the system observable.

## VI. Results and Discussion

The thermal model and thermal state observer are validated by running the battery module with a Worldwide Harmonised Light Vehicles Test Procedure (WLTP) cycle and comparing the measured temperatures with the simulated and estimated temperatures. This comparison can only be done for surface temperatures as core temperature measurements are unavailable. Here we assume that the accuracy of the surface temperature is reflective of the accuracy of the core temperature as the core temperature depends on only one state, the corresponding surface temperature. Hence, if the surface temperature can be simulated/estimated accurately, the core temperature simulation/estimation should also have the same accuracy.

Fig. 10 shows the validation profile for the battery module. The WLTC profile is applied to an electric van and the power demand is scaled to the battery module. The complete profile consists of four cycles of WLTP followed by a resting period (Fig. 10a). A single cycle is shown in Fig. 10b.

The module is instrumented with NTC type temperature sensors at the following locations: Cell 3, 4, 8, 12, 13, 19, 20, 25, 27, 28, 33 and 34, top cooling plate and bottom cooling plate. These sensors can have a potential steady state offset of 1°C and measurement of 0.5°C. Hence, while evaluating the performance of the Thermal Model or TSO an error of 1.5°C is acceptable. The cooling fluid is circulated via the top cooling plate

$$\dot{T}_i^s = -\left[\frac{n_s}{R_{ss}C_{cell}} + \frac{n_a}{R_{sa}C_{cell}} + \frac{2}{R_{sp}C_{cell}}\right] T_i^s + \sum_{j \in \text{adjecent cells}} \frac{T_j^s}{R_{ss}C_{cell}} + \frac{T_T^p}{R_{ps}C_{cell}} + \frac{T_B^p}{R_{sp}C_{cell}} + n_a \frac{T_a}{R_{sa}C_{cell}} + \frac{\dot{Q}_i}{C_{cell}} \tag{23}$$

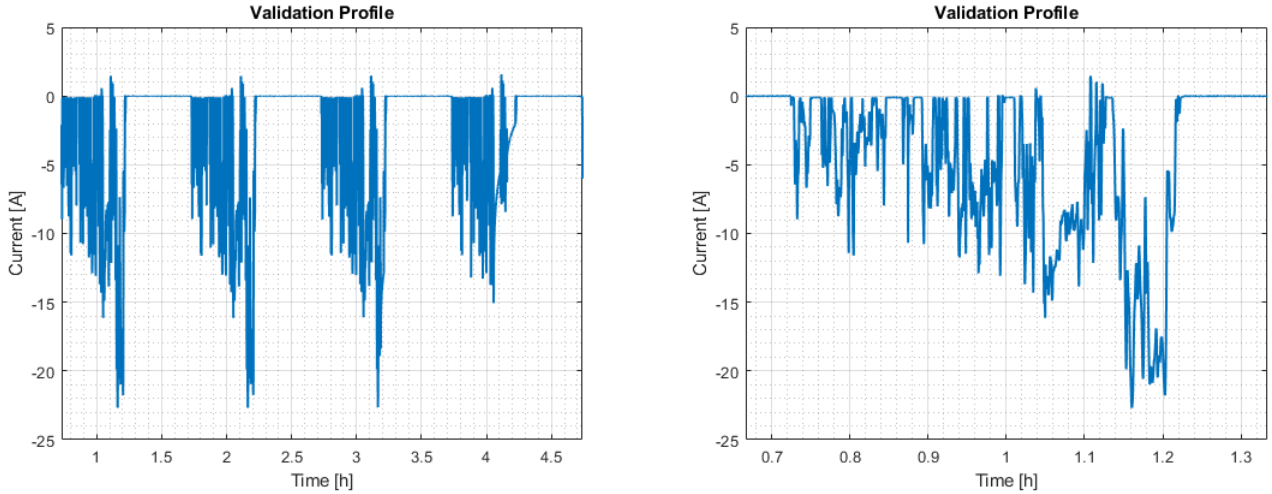


(a) Full Cycle (b) Single Cycle

Fig. 10: WLTC profile for validation tests.

at a temperature of 10°C and a constant flow rate of $8.333 \times 10^{-5}\,\mathrm{m^3\,s^{-1}}$. The module is placed inside a climate chamber which is used to regulate the ambient temperature. The validation test is conducted at $0\,^{\circ}\mathrm{C}$, $20\,^{\circ}\mathrm{C}$ and $40\,^{\circ}\mathrm{C}$ ambient.

### A. Validation of Thermal Model

An open-loop thermal model is simulated by using the input conditions (ambient temperature, fluid temperature, current and voltage) from the validation cycles. The RMS error is calculated for the cells that have temperature measurements. Fig. 11 shows the mean RMS error for different ambient temperatures at each cell. It is seen that the error is higher for cells which are exposed to ambient. This can be explained by the dynamic nature of interaction of the ambient air with these cells. The thermal resistance between the cell and ambient is a lumped parameter describing convective heat release. This can vary more significantly from an identification cycle to a validation cycle due to changes in the conditions of the climate chamber, addition/reduction of sensors or movement in the module. However, the maximum RMS error for all cells remains below 1.6°C.

### B. Validation of Thermal State Observer

For the given system, the TSO is observable if temperature inputs can be obtained from a minimum of 11 cell surfaces and the 2 cooling plates. This leaves one

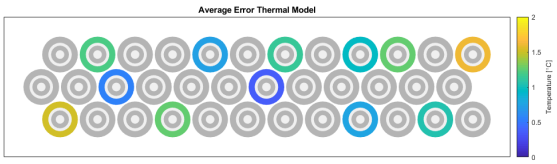


Fig. 11: Mean RMS at each cell for different ambient conditions for feedforward simulation of the Thermal Model.

instrumented cell whose measurement can be used for validation of the temperature estimate. In this work, three different test cases are considered for the validation of the TSO:

- Normal Operation: Denotes a normal operating condition where all sensors working properly.
- Sensor Failure: Is a fault handling case where measurement from one cell is unavailable
- Sensor Malfunction: Is a fault handling case where measurement from one cell has an off-set

For best evaluation of these test cases, Cell 28 is selected for validation of the TSO. It has a relatively high RMS error (Fig. 11). Hence, the benefit of using a TSO to reduce the error can be shown. It is also located adjacent to Cell 25 which is instrumented with

a temperature sensor. This cell can be used to simulate the fault handling capability. A failure/malfunction in the data from an adjacent cell can have immediate impact on the TSO performance. Fig. 12 shows the scheme for the TSO. Here, the temperature from green cells are used as inputs and the temperature of blue cell (Cell 28) is validated.

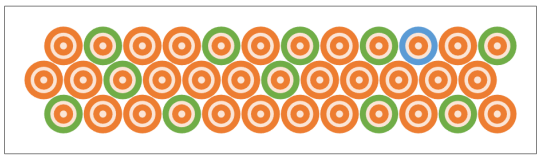

Fig. 12: Temperature sensor placement scheme for evaluation of TSO (Green: TSO input, Blue: Validation).

Fig. 13 shows the result of the state observer during normal operation at an ambient of 40°C. Fig. 13a shows the surface temperature profile of the measurement, model and estimation of Cell 28. It is seen that the estimation is significantly closer to the measurement compared to the model. Fig. 13b shows the error histogram of the model and estimation compared to the measured temperature. The estimation gives a smaller RMS error which is asymptotically decreasing. Despite the asymptotically decreasing error, the RMS error for the TSO is non-zero with a significant off-set. This is explained by the measurement noise present in the data. Since, the estimation is being compared to the measurement, this noise results in the off-set in the RMS error.

The fault handling of the system is simulated by two cases. In the first case, a sensor failure is simulated by removing the measurement from Cell 25 and looking at the deterioration in the RMS error. This also makes the system unobservable. In the second case, a sensor malfunction is simulated by adding an off-set of 20°C to Cell 25 resulting in an unexpected measurement error.

Table III gives the summary of RMS errors for all test cases at all ambient conditions. It is seen that the TSO performance is always better than the model and the error remains below 0.6°C. The sensor failure has little impact on the RMS error, noticeable only at the second decimal place. The sensor malfunction increases the error, but we see an increase of 0.15°C with a measurement error of 20°C. In all operating conditions and at every ambient condition the RMS error of the TSO remains well below 1.5°C (the performance target). Hence, the TSO shows good performance overall.

TABLE III: RMS Error for Cell 28.

| **Ambient** [°C] | **RMS Error** [°C] | | | |
|---|---|---|---|---|
| | **Model** | **TSO** | **Failure** | **Malfunction** |
| 0 | 0.61 | 0.60 | 0.62 | 0.76 |
| 20 | 1.21 | 0.33 | 0.33 | 0.49 |
| 40 | 1.96 | 0.29 | 0.29 | 0.46 |

## VII. Conclusion

In this paper, a modular and scalable thermal model is developed for a cylindrical cell battery module. A methodology is given to identify different parameters of this model. This model is used to develop a Kalman filter based Thermal State Observer (TSO). The performance of the TSO is validated by subjecting the battery module to a series of WLTP profiles. The TSO performance is evaluated for three cases: Normal operation, Sensor failure and Sensor Malfunction. The RMS error of the TSO for all cases is below 1.5°C, the performance target for the algorithm. The core temperature estimates are expected to show similar performance.

## Acknowledgment

This project has received funding from the European Union's Horizon 2020 research and innovation programme under grant agreement No 769935.

## References

[1] https://www.eea.europa.eu/data-and-maps/indicators/transport-emissions-of-air-pollutants-8/transport-emissions-of-air-pollutants-8

[2] Forgez, Christophe, et al. "Thermal modeling of a cylindrical LiFePO4/graphite lithium-ion battery." Journal of Power Sources 195.9 (2010): 2961-2968.

[3] Li, Zhe, et al. "Examining temporal and spatial variations of internal temperature in large-format laminated battery with embedded thermocouples." Journal of Power Sources 241 (2013): 536-553.

[4] Mutyala, Madhu Santosh K., et al. "In-situ temperature measurement in lithium ion battery by transferable flexible thin film thermocouples." Journal of Power Sources 260 (2014): 43-49.

[5] Richardson, Robert R., Peter T. Ireland, and David A. Howey. "Battery internal temperature estimation by combined impedance and surface temperature measurement." Journal of Power Sources 265 (2014): 254-261.

[6] Srinivasan, Rengaswamy, et al. "Instantaneous measurement of the internal temperature in lithium-ion rechargeable cells." Electrochimica Acta 56.17 (2011): 6198-6204.

[7] Srinivasan, Rengaswamy. "Monitoring dynamic thermal behavior of the carbon anode in a lithium-ion cell using a four-probe technique." Journal of Power Sources 198 (2012): 351-358.

[8] Wang, C. Y., and Venkat Srinivasan. "Computational battery dynamics (CBD)—electrochemical/thermal coupled modeling and multi-scale modeling." Journal of power sources 110.2 (2002): 364-376.

[9] Maleki, Hossein, and Ahmad K. Shamsuri. "Thermal analysis and modeling of a notebook computer battery." Journal of Power Sources 115.1 (2003): 131-136.

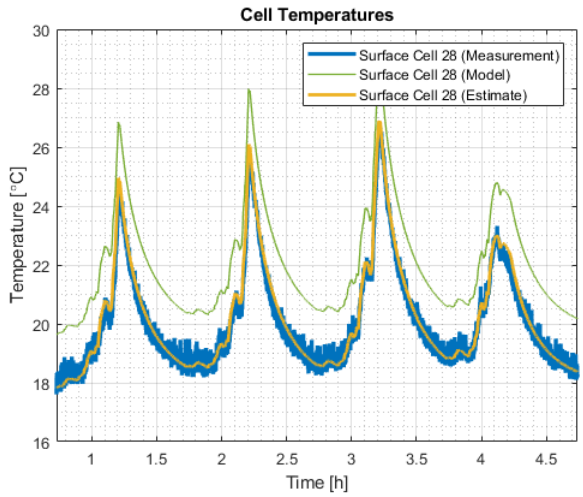


(a) Temperature Profile

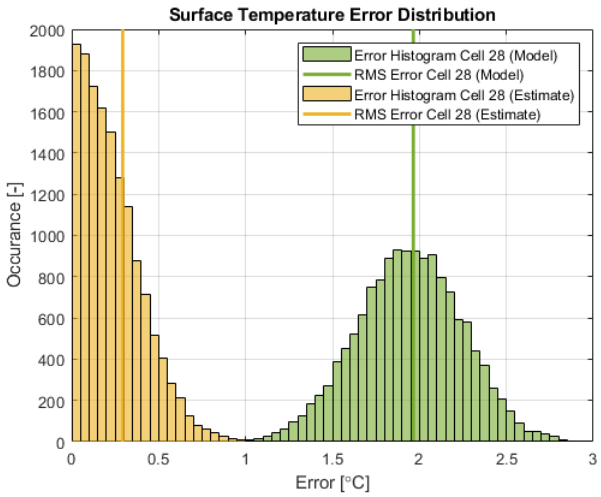


(b) Error Histogram

Fig. 13: TSO performance for Cell 28.


[10] Mahamud, Rajib, and Chanwoo Park. "Reciprocating air flow for Li-ion battery thermal management to improve temperature uniformity." Journal of Power Sources 196.13 (2011): 5685-5696.

[11] Smith, Kandler, and Chao-Yang Wang. "Power and thermal characterization of a lithium-ion battery pack for hybrid-electric vehicles." Journal of power sources 160.1 (2006): 662-673.

[12] Park, Chanwoo, and Arun K. Jaura. Dynamic thermal model of li-ion battery for predictive behavior in hybrid and fuel cell vehicles. No. 2003-01-2286. SAE Technical Paper, 2003.

[13] Abdul-Quadir, Y., Laurila, T., Karppinen, J., Jalkanen, K., Vuorilehto, K., Skogström, L. and Paulasto-Kröckel, M., 2014. Heat generation in high power prismatic Li-ion battery cell with LiMnNiCoO2 cathode material. International Journal of Energy Research, 38(11), pp.1424-1437.

[14] Zhao, R., Zhang, S., Liu, J. and Gu, J., 2015. A review of thermal performance improving methods of lithium ion battery: electrode modification and thermal management system. Journal of Power Sources, 299, pp.557-577.

[15] Kalman, R.E., 1960. A new approach to linear filtering and prediction problems.

[16] Lin, Xinfan, et al. "Online parameterization of lumped thermal dynamics in cylindrical lithium ion batteries for core temperature estimation and health monitoring." IEEE Transactions on Control Systems Technology 21.5 (2012): 1745-1755.